Supporting Information

Hierarchical structure TiNb$_2$O$_7$ microspheres derived from high-performance lithium-ion batteries

Ling Yu, [a] Jintao Lv, [a] Ziwang Zhou, [a] Yafeng Li, *[a] Mingdeng Wei *[a, b]

[a] *Fujian Key Laboratory of Electrochemical Energy Storage Materials, Fuzhou University, Fuzhou, 350002, Fujian, China.*
[b] *State Key Laboratory of Photocatalysis on Energy and Environment, Fuzhou University, Fuzhou, 350002, Fujian, China.*

E-mail address: liyf@fzu.edu.cn; wei-mingdeng@fzu.edu.cn;

Experimental Section

Synthesis of amorphous titanate precursor

0.5 g of TiO_2 (P25) was dispersed in a 50 mL of 10 M NaOH solution (H_2O:EtOH V/V=1:1). After stirring for 30 minutes, the obtained white suspension was transferred into 100 mL of autoclave and heated at 200 ℃ for 24 h. The resulting product was washed with 0.1 M HNO_3 until the pH 1-2. After stirring in 0.1 M HNO_3 for 24 h, the product was centrifuged with deionized water until pH 7-8 was reached, finally dried under 70 ℃ for 12 h in the oven.

Synthesis of TNO-MS and TNO-NP

0.2 g of $NbCl_5$ was dissolved in HCl-EtOH (V/V=0.2:30) with intensive stirring. Until the solution changes from yellow to colorless, 55 mg of amorphous titanate precursor was mixed into the above solution. After stirring for 20 min, the obtained white suspension was transferred into the 50 mL Teflon-lined stainless steel autoclave. After heating at 200 ℃ for 12 h, the precursor was washed with deionized water and ethanol over three times and dried at 70 ℃ in oven for 12 h. The precursor was calcined at a high temperature of 800 ℃ for 2 h in argon atmosphere to obtained $TiNb_2O_7$ microspheres (named as TNO-MS). The same procedure was also used to prepare the reference substance $TiNb_2O_7$ nanoparticles in addition to the absence of hydrochloric acid (name as TNO-NP).

Structural characterization

Rigaku Ultima IV X-ray diffraction (XRD, Cu K$_\alpha$ radiation) was used to analyze the crystal structure of the prepared material at 40KV and 20mA. The Raman spectra were recorded on a Renishaw Invia Raman microscope with a laser wavelength of 532nm. The BET surface area was performed by Micromeritics ASAP 2020 instrument (Micromeritics, Norcross, GA, USA). The morphologies of the samples were characterized by scanning electron microscope (SEM, Hitachi S4800 instrument) and a transmission electron microscope (TEM, FEI F20 S-TWIN 0 instrument). XPS (ISCALAB 250) was employed to investigate the elements valence and bonding state of materials. The electron paramagnetic resonance (EPR) signal was recorded on A300 Electron Paramagnetic Resonance Spectroscopy.

Electrochemical measurement

The working electrode consisted of TNO-MS or TNO-NP powders, acetylene black, and binder of sodium alginate at a weight ratio of 7:2:1 with the distilled water as the solvent. The obtained uniform slurry was coated on the copper foil as working electrodes and transferred to a vacuum oven for 12 hours at 110 ℃. The CR2025 cells were assembled in a glove box filled with highly pure argon gas. Whether in full-cell or half-cell, 1 M $LiPF_6$ in EC/EMC/DMC (1:1:1 by volume) was used as the electrolyte. Electrochemical properties of materials were tested by using pure lithium metal (Aldrich) as the counter electrode in the half-cell. For full cell, $LiFePO_4$ cathode was containing commercial $LiFePO_4$ (80 wt%), acetylene black (10 wt%), and PVDF binder (10 wt%), and Al foil was employed as a current electrode. The weight ratio of the cathode and anode materials was about 2:1. The capacity of the full-cell was calculated based on the weight of the anode active material. Cycling voltammetry and charge-discharge measurements were performed using a CHI 660D electrochemical workstation and NEWARE (CT-4008), respectively.

The specific steps of pre-lithiation treatment

First, the Cu foil coated with anode material was assembled into a half-cell with charging-discharging three times at 0.2 A g^{-1}. Second, the battery was disassembled and the Cu foil coated with anode materials was taken out and washed with ethanol, then dried in a vacuum oven at 60 °C overnight. Finally, the Cu foil coated with anode materials was assembled into coin-cells again, and a series of electrochemical tests were performed after quiescence 12 h. This step also be required when the assembly of full-cell.
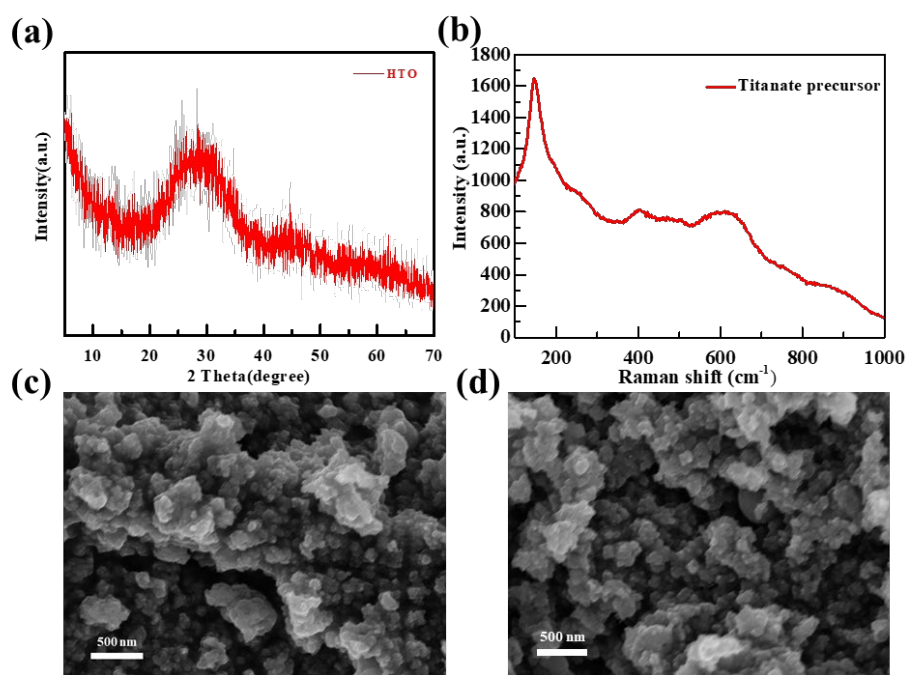
Fig. S1 (a) XRD pattern, (b) Raman spectrum, (c-d) SEM image of amorphous titanate precursor.
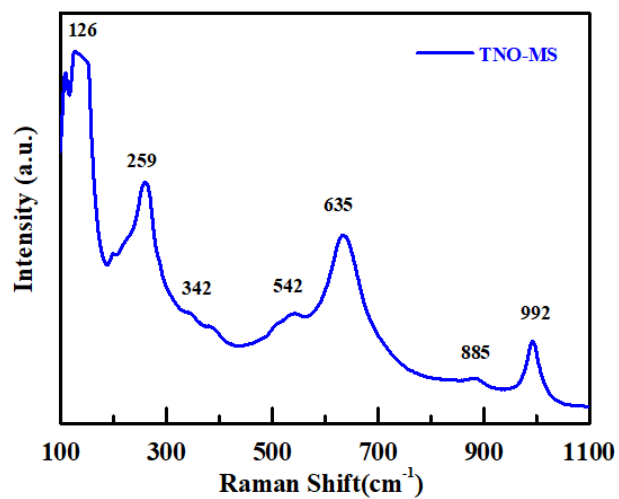
Fig. S2 Raman spectrum of TNO-MS.
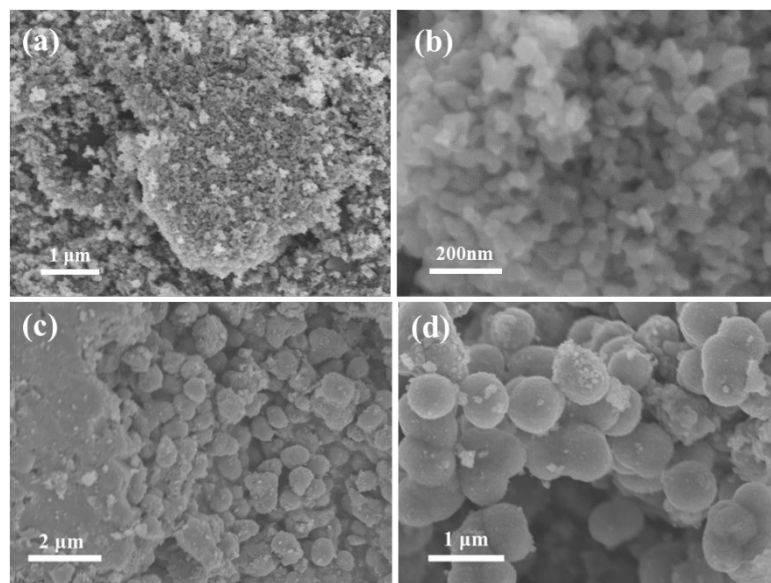
Fig. S3 (a-b) SEM images of TNO-NP, (C) SEM image of TiNb$_2$O$_7$ prepared by 0.1 ml hydrochloric acid and (d) SEM image of TiNb$_2$O$_7$ prepared by acetic acid.

.
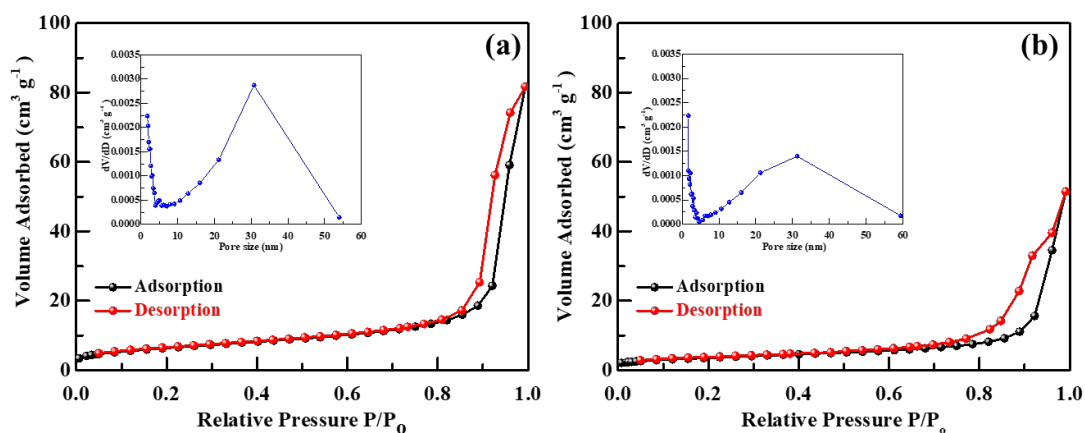
Fig. S4. N_2 adsorption-desorption isotherms and the corresponding pore size distribution (inset) of the (a) TNO-MS and (b) TNO-NP.

As shown in Fig. S4, N_2 adsorption-desorption isotherms show that the specific surface area of TNO-MS and TNO-NP is 22.8 m^2 g^{-1} and 12.7 m^2 g^{-1}, respectively. The difference in specific surface area between the two materials is so close, this may be related to the fact that the primary units of the two materials are both nanoparticles. The inset of Fig. S4 also indicates that both samples were mesoporous materials with the pore size distribution ranging from 2 nm to 50 nm. The pore volume of TNO-MS is 0.11 cm^3 g^{-1}, while the pore volume of TNO-NP is only 0.05 cm^3 g^{-1}, proving that the hierarchical structure is beneficial to the permeation of electrolyte solution
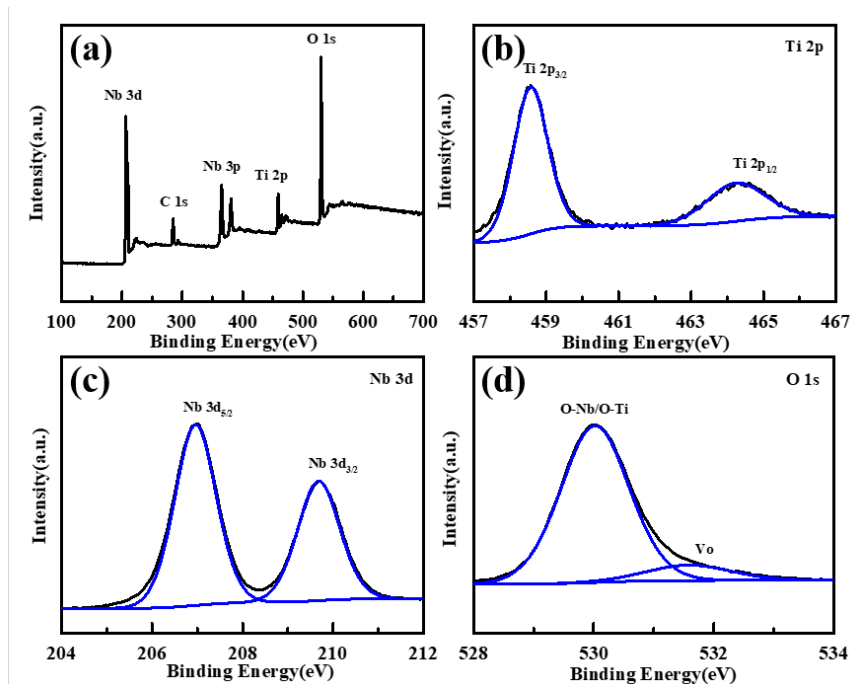
Fig. S5 The full XPS spectrum of (a) TNO-MS, high-resolution spectra for (b) Ti 2p, (c) Nb 3d, and (d) O 1s of TNO-MS.

The atomic arrangement and electronic configuration of the electrode materials play a crucial role in the electrochemical properties of lithium-ion electrode materials. Herein, XPS was employed to investigate the elements valence and bonding state of the TNO-MS. Fig. S5a shows the full spectrum of the TNO-MS, and demonstrates that this material only consisted of Ti, Nb, and O elements. The peaks appearing at 458.58 and 464.28 eV correspond to $2p_{3/2}$ and $2p_{1/2}$ of Ti, respectively (Fig. S5b), indicating the Ti^{4+} oxidation state in TNO-MS. In Fig. S5c, the Nb 3d spectrum exhibits two peaks at 206.98 ($Nb\ 3d_{5/2}$) and 209.68 eV ($Nb\ 3d_{3/2}$), which are confirmed to the characteristic peaks of Nb^{5+}. The peaks of the O 1s are located at 529.98 eV and 531.58 eV, corresponding to the O-M (M=Ti, Nb) bond and oxygen vacancies (V_O), respectively (Fig. S5d).
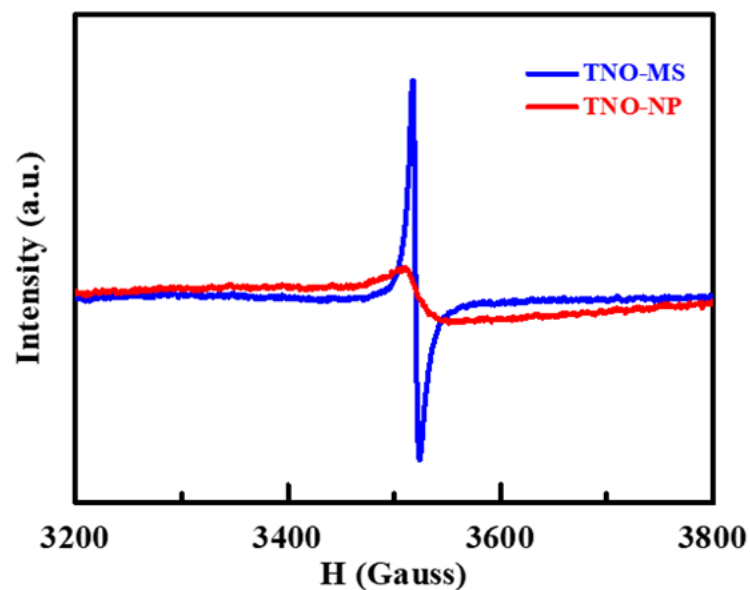
Fig. S6 EPR spectra of TNO-MS and TNO-NP.

As shown in Fig. S6, the EPR spectrum of TNO-MS exhibits a distinct signal at about g=2.02, clearly illustrating the existence of oxygen vacancies. By comparing the signal peak intensity of two samples, indicating that more oxygen vacancies might be introduced in this process due to the intervention of hydrochloric acid.
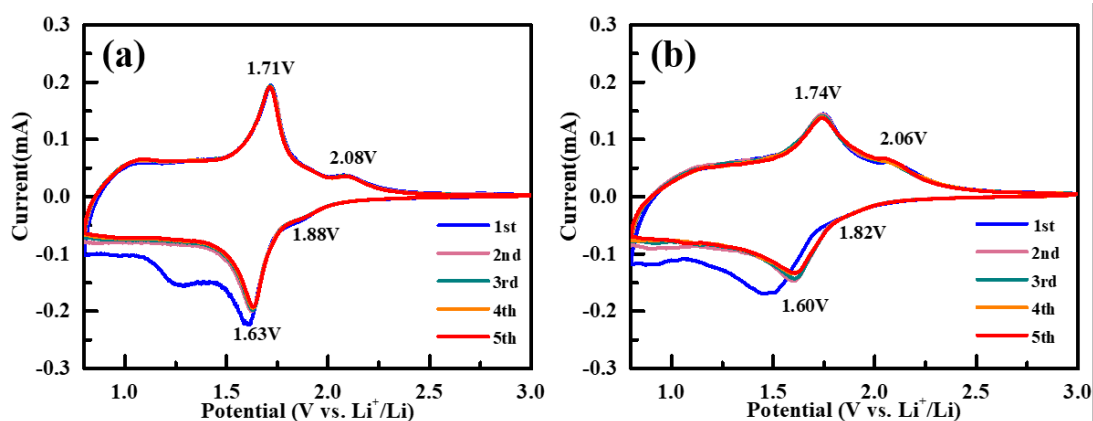
Fig. S7 CV curves of (a) TNO-MS and (b) TNO-NP electrode for the first five cycles between 0.8-3 V at 0.2 mV s^{-1}.

To further illustrate the electrochemical reaction of the electrode material, cyclic voltammograms (CV) of the initial five cycles for the TNO-MS and TNO-NP anodes were measured at a rate of 0.2 mV s^{-1} in the potential range of 0.8-3.0 V. As illustrated in Fig. S7(a-b), all of the CV curves are highly consistent with the previous reports. In the case of the TNO-MS, one pair of obvious redox peaks at 1.63/1.71 V can be attributed to the redox of Nb^{5+}/Nb^{4+}. At the same time, an irreversible broad bump in the range of 1.1-1.4 V in the initial cycle could be associated with the valence variation of the partial Nb^{4+}/Nb^{3+} in anode materials. In addition, there is an additional inconspicuous redox pair located at 1.88/2.08 V, corresponding to the valence variation of Ti^{4+}/Ti^{3+}. Compared with the same active materials mass of reference sample TNO-NP, the CV curves of TNO-MS present smaller potential difference between the redox couples and larger peak current value, indicating that this material has a better electrochemical kinetic. Meanwhile, the better superimposition of the CV curves from the second cycle to the fifth cycle also illustrates that TNO-MS has preferable reversibility as an anode for LIBs.
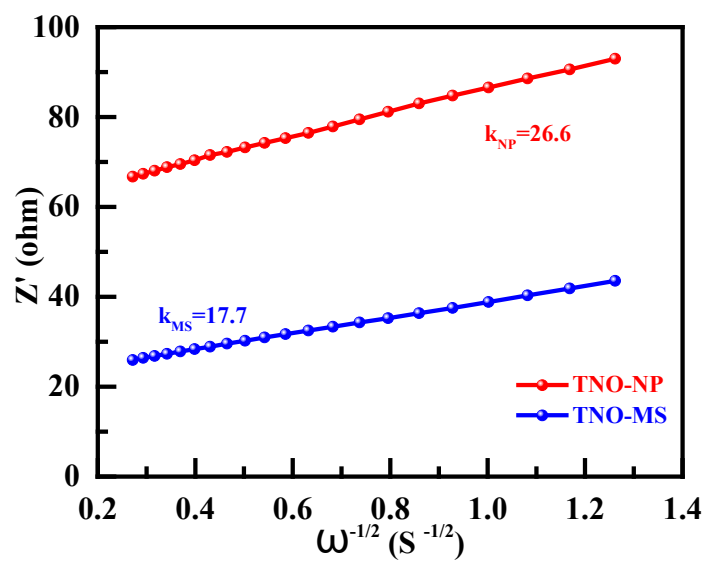
Fig. S8 The relationship between Z' and $\omega^{1/2}$.
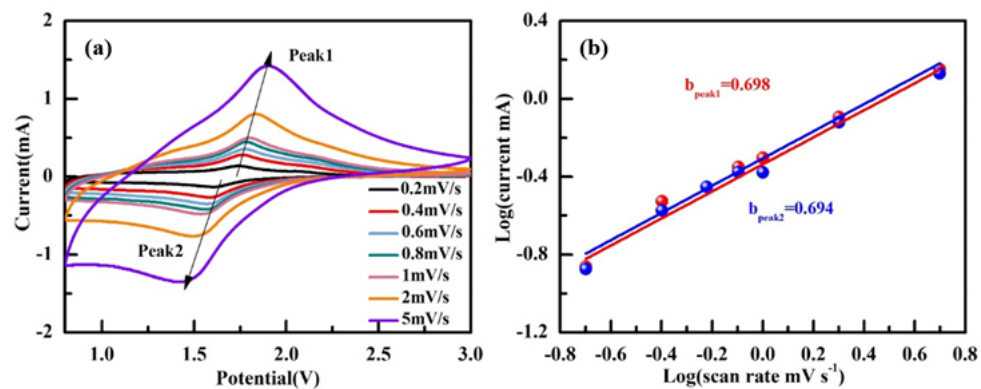
Fig. S9 (a) CV curves of TNO-NP at various scan rates from 0.2 to 5 mV s^{-1}, and (b) the relationship between the peak current and the scan rate in the logarithmic form.
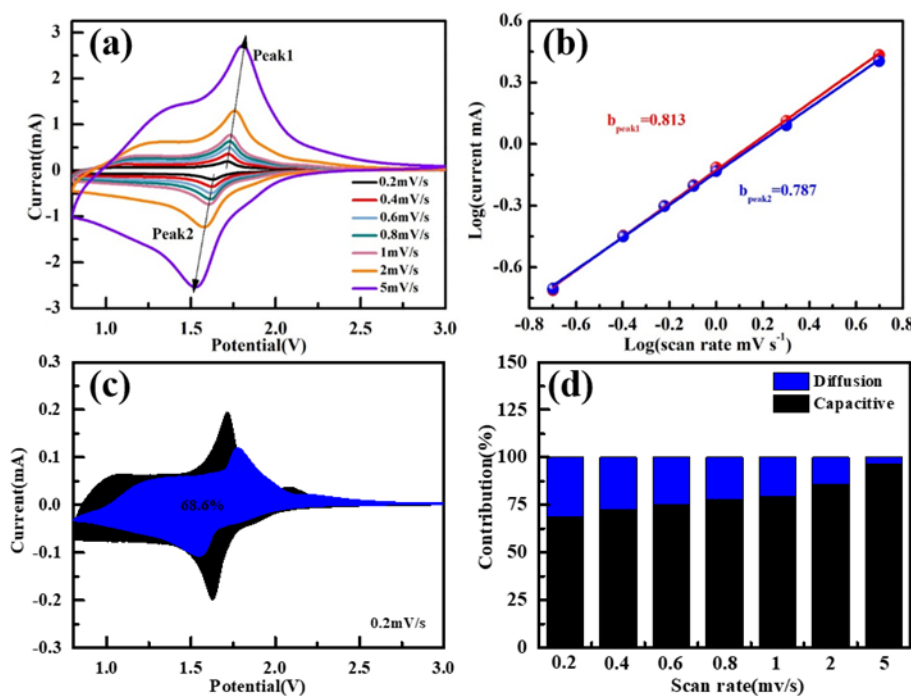
Fig. S10 (a) CV curves at various scan rates from 0.2 to 5 mV s^{-1}, (b) the relationship between the peak current and the scan rate in the logarithmic form, (c) the ratio of capacitive and diffusion contribution of TNO-MS electrode at scan rate of 0.2 mV s^{-1} and (d) contribution ratio of the capacitive and diffusion-controlled charge at various scan rates for TNO-MS.

The energy storage process can be simply divided into two parts, i) pseudocapacitive behavior controlled by the surface, and ii) diffusion-controlled process. In the process of charge-discharge, if the proportion of pseudocapacitive behavior is higher, which means that the material can exhibit better electrochemical performance in the process of rapid intercalation/extraction of Li$^+$. Fig. S9a and Fig. S10a separately provide the CV curves of the two electrodes at the sweep rates from 0.2 to 5 mV s^{-1}. The relationship between the current (i) and the scan rate (v) can be characterized according to the equation (1):

$$i=av^b \tag{1}$$

where a and b are all adjustable parameters. The value of b gets closer to 1, indicating that the electrochemical process is more controlled by capacitive behavior. While the value of b approaches 0.5, manifesting that the electrochemical system is contributed by the diffusion process. As shown in Fig. S9b and Fig. S10b, it can clearly be seen that the b values of TNO-MS are much higher than those of TNO-NP, demonstrating that the contribution of pseudocapacitive behavior dominated the charge-discharge process, which also accounts for the excellent rate performance of TNO-MS.

Two different contributions can be quantified using the equation (2):

$$i=k_1v+k_2v^{1/2} \tag{2}$$

where the current i is made up of two parts, k_1v and $k_2v^{1/2}$, corresponding to the pseudocapacitive behavior and diffusion process, respectively. As a result, the proportion of pseudocapacitive contribution can be calculated by k_1v. As shown in the blue part region in Fig. S10c, the pseudocapacitive contribution of TNO-MS accounts for 68.6% at 0.2 mV s^{-1}. Fig. S10d ulteriorly displays the changes in the proportions of the pseudocapacitive contribution and the diffusion contribution at different scan rates. The quantified results manifest that the contribution of pseudocapacitive behavior increased with increasing scan rates, with percentages of 96.75% at 5 mV s^{-1}.

Table S1. Comparisons of reversible capacity of TNO-MS with other intercalation-type oxide anode materials for full-cell.

Sample	Cycling performance	Rate capability	References
Carbon coated porous titanium niobium oxides	80.5% @ 6C after 500 cycles	133.7 mA h g^{-1}@ 6 C	ACS Appl. Mater. Inter., 2020, **3**, 5657-5665.
$V_3Nb_{17}O_{50}$	85.7% @ 5C after 500 cycles	61 mA h g^{-1}@ 10 C (1C= 423 mA g^{-1})	Energy Storage Mater., 2020, **30**, 401-411
$MoNb_{12}O_{33}$	93.9% @ 5 C after 1000 cycles	95 mA h g^{-1}@ 10 C (1C=401 mA g^{-1})	J. Mater. Chem. A, 2019, **7**, 6522-6532
V^{5+}-doped $TiNb_2O_7$ microspheres	82.4 mA h g^{-1} @ 1.5 C after 200 cycles	89.3 mA h g^{-1}@ 1.4 C (1C=387.6 mA g^{-1})	Chem. Eng. J., 2020, **407**, 127190
$HfNb_{24}O_{62}$	84.7% @ 5 C after 500 cycles	78 mA h g^{-1}@ 10 C (1C=378 mA g^{-1})	Chem. Commun., 2019, **56**, 619-622
This work	77.9% @ 2 A g^{-1} after 2000 cycles	127.8mAh g^{-1}@ 5 A g^{-1}	